Modelling the reopening of liquid-lined lung airways

O. E. Jensen & M. K. Horsburgh
Centre for Mathematical Medicine, School of Mathematical Sciences, University of Nottingham, Nottingham NG7 2RD, UK

Abstract

Airway reopening is the process whereby a bubble of air is blown into a liquid-filled lung airway, peeling apart the wet airway walls. It has relevance to the first breath, ventilator-induced lung injury and a variety of pulmonary diseases. Reopening has been studied intensively through simplified physical models, in which an airway is represented by either a thin-walled elastic tube or a pair of spring-backed membranes under longitudinal tension. Theoretical studies of these systems are reviewed, and a new model is examined in detail which accounts for weak permeability of the airway wall. Using matched asymptotic expansions to obtain a relationship between the bubble pressure and the speed of steady reopening, it is shown how wall permeability allows for a mode of slow, steady reopening not found in the impermeable-wall case.

1 Introduction

The liquid lining of peripheral lung airways is normally very thin, but if it is sufficiently thick it can readjust via a surface-tension-driven instability to form an occlusive liquid bridge (Figure 1a,b) [9, 10, 21]. This is an important mechanism of 'airway closure', and it is physiologically significant because gas exchange will be impaired unless the airway can be reopened rapidly. Airway deformability promotes this instability since locally low capillary pressures in a liquid bridge can cause the airway to buckle and collapse (Figure 1c) [11, 14], increasing the proportion of the airway that is blocked with liquid.

Reopening a collapsed and partially flooded airway is therefore a process of fundamental importance in pulmonary mechanics. Observations in animal

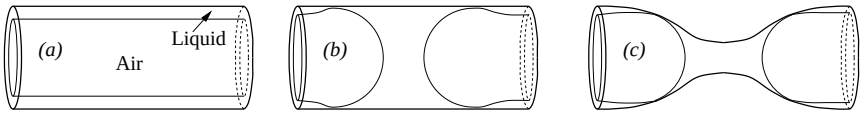

Figure 1: An initially uniform liquid lining of a cylindrical airway (a) can be destabilised by surface tension to form a liquid bridge (b); low pressure in the bridge can cause local airway collapse (c).

models [24, 28, 36] support the view that reopening occurs by an air bubble advancing into a collapsed airway and peeling apart wet airway walls. Since viscous and surface-tension forces contribute to the adhesive forces that resist reopening, elevated levels of airway closure are common in diseases in which the liquid lining is excessively viscous (such as cystic fibrosis) or in which the liquid lining has abnormally high surface tension (such as respiratory distress syndrome arising from surfactant deficiency). Prolonged airway closure is also a problem in emphysema, where airway walls are unusually compliant and prone to collapse.

Possibly the most dramatic example of airway reopening occurs at the time of the first breath. Infants are born with their lungs full of fluid, yet they are normally able to draw air into their lungs within seconds of birth. The surface-tension-lowering properties of pulmonary surfactant play an important role in enabling this to occur. For severely premature infants lacking adequate quantities of surfactant, however, artificial ventilation (alongside surfactant replacement therapy) may be required to assist the first breath and can be required for days or weeks thereafter. Conventional mechanical ventilation, which operates at normal breathing rates and uses large tidal volumes, can lead to repeated opening and closing of small airways. The associated stresses exerted on delicate airway walls can lead to chronic lung damage [6]. It is therefore of value to understand the physical conditions under which an airway can be reopened, and the resulting stresses that reopening imposes on airway epithelium.

Bench-top experiments by Gaver, Samsel & Solway [7], in which polythene tubes lined with viscous fluid were inflated by a bubble of air (similar to the arrangement shown in Figure 2), were the first to characterize the major physical effects controlling airway reopening. They showed that the pressure p_b^* of a propagating bubble had to be in excess of a yield value in order for the bubble to advance steadily along the tube: this yield pressure was found to be proportional to γ/D^*, where γ is the surface tension of the liquid and D^* the half-width of the inflated tube. A similar threshold was found in an animal study by Naureckas *et al.* [28]. For p_b^* above the yield pressure, Gaver *et al.* found that the bubble propagation speed U^* increased monotonically with p_b^*. Varying γ, the viscosity μ of the liquid, the fluid volume and the longitudinal tension of the tube, they found that data from multiple experiments collapsed onto a roughly universal rela-

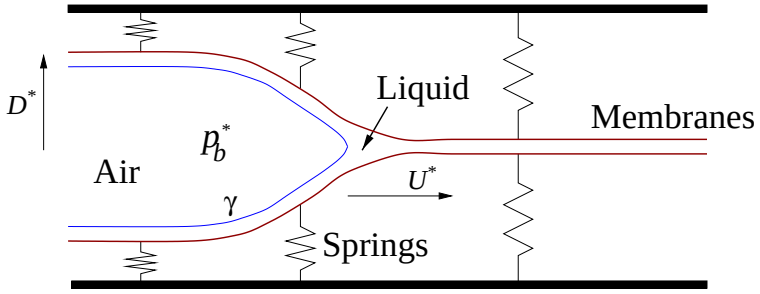

Figure 2: One of the physical models used in bench-top experiments. A bubble at pressure p_b^* advances from left to right with speed U^* into a liquid-filled channel. Liquid of viscosity μ and surface tension γ lies between two membranes that are held under tension and are supported externally by springs.

tionship if they plotted the dimensionless pressure $p_b = p_b^* D^*/\gamma$ against the dimensionless speed (the capillary number) $Ca = \mu U^*/\gamma$. To avoid the complications of a fully three-dimensional geometry, subsequent experiments by Perun & Gaver [30, 31] used systems in which the tube was replaced by a planar deformable channel, in which external springs were used to mimic the effects of circumferential hoop stresses (Figure 2). Driving the bubble with a constant-flow source, they showed how p_b^* can exhibit a transient overshoot during the initiation of airway reopening, before settling to its steady-state value. Again, they found a monotonic relation between p_b and Ca. They also used their physical model to mimic the tethering of airways to surrounding parenchyma [31] and, following animal studies by Yap *et al.* [36], showed how the yield pressure could be reduced by increased tethering.

The first theoretical model of airway reopening was developed by Gaver *et al.* [8], using the configuration shown in Figure 2. Solutions for a steadily propagating bubble at zero Reynolds number were computed using a hybrid numerical scheme coupling the boundary-element method (a technique well suited to Stokes flows with free surfaces) to lubrication theory (which is used to describe the flow at either end of the computational domain where the aspect ratio of the flow domain is large). An approximate model coupling lubrication theory to capillary statics was also used to validate solutions at low Ca. Steady solutions were characterized by the relationship between the dimensionless bubble pressure p_b and bubble speed Ca. Computations demonstrated the existence of two steady solution branches (Figure 3). The left-hand branch has p_b decreasing with increasing Ca (contrary to experiment), with the channel widely inflated ahead of bubble tip; this was called the 'pushing' mode in [8]. The right-hand branch has p_b increasing with Ca (as in experiment); since the bubble has a more pointed tip this was called the 'peeling' mode. The pressure at the minimum of the p_b–Ca curve

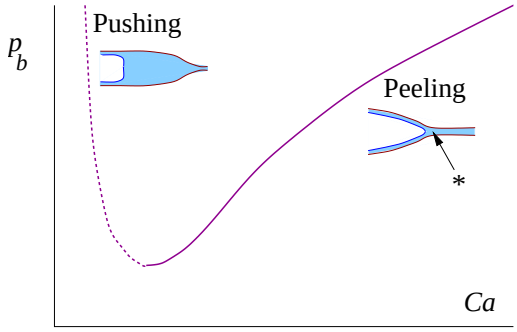

Figure 3: Steady reopening of a channel with impermeable walls, showing dimensionless bubble pressure $p_b = p_b^* D^*/\gamma$ versus bubble speed $Ca = \mu U/\gamma$. Insets show typical solution shapes for each solution branch. The point denoted with $*$ is where the liquid pressure in the channel is lowest.

provides a good candidate for the yield pressure seen experimentally. Later computations [20] showed excellent agreement between the branch of peeling solutions and experimental results of Perun & Gaver [31]. The pushing mode has not been observed experimentally, although Bretherton's [3] approximation of slow bubble motion in a parallel-sided channel can be used to explain its apparently anomalous pressure-speed relationship ($p_b \propto Ca^{-2/3}$ for $Ca \ll 1$).

An asymptotic approximation for both branches of the pressure-speed relationship was provided by Jensen *et al.* [20]. The approximation relies on the realistic assumption that the membrane's longitudinal tension is large, and that membrane slopes are uniformly small. The flow can then be split into three distinct regions. A few channel widths ahead of bubble, the channel is well described by lubrication theory. Behind bubble tip, the liquid film sits almost passively on channel wall, and the membrane is in approximate equilibrium. Surface tension is important only in the remaining region surrounding the tip of the bubble. This region has an aspect ratio of order unity, and the flow is inherently two-dimensional. Because the membrane slope is small, however, the membranes are locally almost flat and parallel, and so the flow here is equivalent to that of a bubble advancing in a planar channel. This so-called 'Bretherton problem' is well-studied and is parameterized by the bubble speed Ca alone; numerical solutions are available for a full range of Ca. Jensen *et al.* [20] showed how solutions of the Bretherton problem can be matched to approximations for the two neighbouring regions, reducing the full reopening problem from PDEs with nonlinear free boundaries to a nonlinear eigenvalue problem involving a third-order nonlinear ODE, from which the relationship between p_b, Ca and the remaining material parameters can be readily obtained. The analysis includes a cor-

rection accounting for the fact that the membranes near the bubble tip are flat but slightly non-parallel (so that the bubble is effectively entering a converging, wedge-shaped channel), taken from an independent computational study by Halpern & Jensen [12]. The approximation in [20] gives excellent agreement with computational results, capturing both the pushing and peeling modes and the turning point of the solution curve (as in Figure 3). Further simplifications are possible if the width of the fluid-filled channel ahead of the bubble is much smaller than the width D^* of the inflated region: in this case there is a strong analogy with the peeling motion described by McEwan & Taylor [26], and the pressure-speed relation can be given by an explicit formula.

The relative simplicity of steady peeling motion provides us with a reasonably clear picture of the physical processes controlling airway reopening. A short distance ahead of the bubble tip the membrane is highly curved, and since the membrane tension is large the liquid pressure near the sharp bend in the membrane is very low (see the point indicated with an asterisk in Figure 3). Increasing the bubble pressure increases the peeling angle, sharpens the bend in the membrane and lowers the liquid pressure further. This low pressure resists the peeling apart of the two membranes, and controls the rate at which reopening can advance. Since the liquid pressure is substantially greater in magnitude than the bubble pressure, the biggest stresses exerted on the walls of the channel are (surprisingly) inward normal stresses, although they act on a given section of membrane only transiently. Whether this simple picture applies directly to lung airways *in vivo* remains to be demonstrated experimentally.

An important aspect of peeling motion that remains poorly understood is that of unsteadiness. This is significant because the transient overshoot in p_b^* seen experimentally [30, 31] during the initiation of reopening could translate to dangerously large stresses being exerted during mechanical ventilation if airways are reopened too rapidly. To explore the origin of this behaviour, Horsburgh [16] and Naire & Jensen [27] extended the asymptotic model in [20] to include unsteady effects. This extended model was used to verify the stability of peeling motion (and the instability of pushing motion) when p_b is held fixed, results which have been corroborated by full Stokes-flow simulations (D. Halpern, personal communication). Prescribing instead a steady increase of bubble volume, the model successfully reproduced transient overshoots in p_b. This occurs because, on initial inflation, the bubble widens before it starts to lengthen. At low bubble fluxes, recent simulations by S. Naire and D. Halpern show that bubble growth can occur in an oscillatory fashion, with low-speed widening (in the pushing mode) alternating with rapid lengthening (in the peeling mode).

Six additional physical effects that are likely to be relevant to airways have also been investigated. First, surfactants, either present naturally or delivered therapeutically, can alter the detailed flow structure near the bubble tip via Marangoni effects (flows driven by gradients of surface tension).

Surfactants can therefore control the rate at which fluid can escape past the bubble tip, and hence have a direct influence on reopening pressures. The effect of soluble surfactant in bulk equilibrium has been described by Yap & Gaver [35]: a wide range of further behaviours remains to be investigated. Second, Heil [15] has shown that inertial effects can be significant in reopening and that there can be a significant increase in p_b for a given Ca, even at moderate Reynolds numbers. Third, he also replaced the *ad hoc* wall model illustrated in Figure 2 with a more rationally based Lagrangian membrane, but found broadly similar behaviour to that found in [8] if inertia was neglected. Fourth, Hazel & Heil [13] have extended these studies to three dimensions, using highly efficient finite element methods to solve for the advance of a bubble into a non-axisymmetrically buckled elastic tube. Results show that despite the increased geometrical complexity, the picture of pushing and peeling motions shown in Figure 3 carries over to the full three-dimensional problem. Fifth, while all the experimental and theoretical studies mentioned so far have involved Newtonian liquids, airway liquids are almost certainly non-Newtonian: some of the effects of non-Newtonian liquid properties on the pressure-speed relationship during reopening have been characterized experimentally [18, 19, 23]. Sixth, an important long-term goal in this area is to relate bubble motion in an individual airway to the inflation of a bifurcating network of connected airways. There remains a substantial gulf between the detailed airway-scale models described above and the statistical-mechanical lung-scale models developed by Suki and co-workers [1, 32, 33], for example.

The remainder of this chapter concerns a further effect that is of potential physiological importance: airway wall permeability. Liquids cross airway epithelium by both active and passive mechanims (fetal lung liquid is actively pumped out of airways during labour, for example [2]); here we consider the effect of passive permeability on the basic airway reopening phenomenon. We explore solutions with a fundamentally different structure to those described so far: we imagine that the advancing meniscus acts like a piston, pushing fluid ahead of it and sideways out through the channel walls. We will show how this solution connects with the impermeable pushing and peeling solutions if the bubble advances too fast for fluid to escape through the walls. A summary of the results presented below is given in [17].

2 A model of permeable airway reopening

In order to investigate the effect of airway wall permeability on airway reopening, we adopt a simple extension of the physical model employed in [8], as illustrated in Figure 4.

This model consists of a liquid-filled, two-dimensional, flexible-walled channel that is opened by an inviscid, semi-infinite bubble. The walls of the channel are modelled as membranes held under tension T^* and supported by

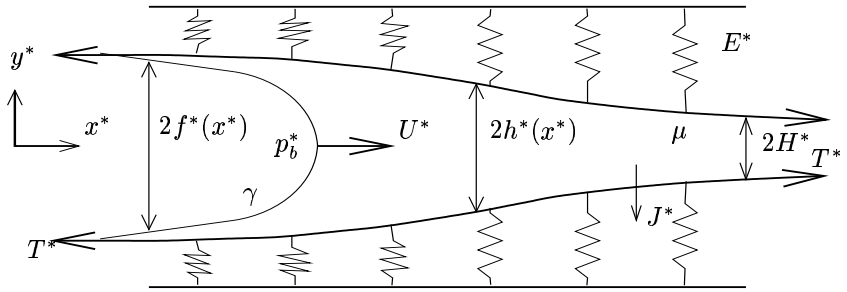

Figure 4: Permeable airway reopening model

linearly elastic springs with stiffness E^*. The separation of the membranes in stress-free conditions is $2H^*$. The liquid is assumed Newtonian with viscosity μ. The surface tension of the interface between the air and the liquid is γ, assumed uniform. We seek steady solutions in which the meniscus is propagating at a fixed speed U^*, driven by a constant pressure within the bubble, p_b^*. We adopt a Cartesian coordinate system (x^*, y^*) with the origin fixed at the bubble tip and x^* directed along the channel centreline. The channel walls move tangential to themselves in this reference frame. The membranes lie at $y^* = \pm h^*(x^*)$ and the meniscus at $y^* = \pm f^*(x^*)$ in $x^* \leq 0$, where $f^*(0) = 0$.

The key difference between the present model and that in [8] is the inclusion of membrane permeability. This is governed by Starling's law of membrane filtration

$$J^* = K^* \left(p^* - \Pi^*\right), \tag{1}$$

which relates the transmural flux J^* to the difference between the fluid pressure p^* at the membrane and the osmotic pressure Π^*. K^* is the permeability of the membrane. The mechanical pressure is taken to be zero outside the channel, and the osmotic pressure is assumed to be zero within the channel, since in normal airways the concentration of proteins is much higher in the interstitium than in the airway lumen. This transepithelial protein concentration difference can generate osmotic pressure differences of more than 10 cm H_2O [2], which can be a significant fraction of airway reopening pressures.

2.1 Governing equations

We assume that the Reynolds number of this flow is small, so that inertial effects may be neglected. Defining nondimensional variables (indicated by tildes) with respect to the length scale H^*, the velocity scale U^* and the viscous pressure scale $\mu U^*/H^*$, the governing Stokes and continuity equations are

$$\tilde{\nabla} \cdot \tilde{\mathbf{u}} = 0, \qquad \tilde{\nabla}\tilde{p} = \tilde{\nabla}^2 \tilde{\mathbf{u}} \tag{2}$$

where $\tilde{\mathbf{u}}(\tilde{x},\tilde{y}) = (\tilde{u},\tilde{v})$ is the velocity field of the liquid.

The effects of surfactants are neglected, so that the meniscus is assumed not to sustain any interfacial shear stress, although there is a pressure drop across the interface due to surface tension. The interfacial stress condition is therefore

$$\tilde{\sigma}\cdot\mathbf{n} = -\left(\frac{1}{Ca}\tilde{\kappa}_{\text{meniscus}} + \tilde{p}_b\right)\mathbf{n} \qquad \text{on} \qquad \tilde{y} = \tilde{f}, \tag{3}$$

where $Ca = \mu U^*/\gamma$, $p_b^* = (\mu U^*/H^*)\tilde{p}_b$, $\tilde{\sigma} = -\tilde{p}\mathbf{I} + (\tilde{\nabla}\tilde{\mathbf{u}} + \tilde{\nabla}\tilde{\mathbf{u}}^T)$ is the fluid stress tensor, $\mathbf{n} = (\tilde{f}_{\tilde{x}}, -1)/(1+\tilde{f}_{\tilde{x}}^2)^{1/2}$ is the liquid outward-facing normal and $\tilde{\kappa}_{\text{meniscus}} = \tilde{f}_{\tilde{x}\tilde{x}}/(1+\tilde{f}_{\tilde{x}}^2)^{3/2}$ is the meniscus surface curvature. Here subscripts $\tilde{x}$ denote derivatives. The kinematic condition on this interface (which is stationary in the bubble-tip reference frame) is

$$\tilde{\mathbf{u}}\cdot\mathbf{n} = 0 \qquad \text{on} \qquad \tilde{y} = \tilde{f}. \tag{4}$$

The vertical normal stress at the membrane due to the fluid is balanced by membrane tension and compression of the springs, so that

$$-\mathbf{m}\cdot\tilde{\sigma}\cdot\mathbf{m} = -\tilde{T}\tilde{\kappa}_{\text{membrane}} + \tilde{E}(\tilde{h}-1)m_y \qquad \text{on} \qquad \tilde{y} = \tilde{h}. \tag{5}$$

Here $\tilde{T} = T^*/\mu U^*$ measures the strength of the membrane tension relative to viscous forces, and $\tilde{E} = E^* H^{*2}/\mu U^*$ measures spring stiffness relative to viscous forces; $\mathbf{m} = (m_x, m_y) = (-\tilde{h}_{\tilde{x}}, 1)/(1+\tilde{h}_{\tilde{x}}^2)^{1/2}$ is the liquid outward-facing normal and $\tilde{\kappa}_{\text{membrane}} = \tilde{h}_{\tilde{x}\tilde{x}}/(1+\tilde{h}_{\tilde{x}}^2)^{3/2}$ is the membrane surface curvature. The membrane is assumed to be massless and dissipation-free, and we assume that the shear stress on the membrane does not induce any significant variation in the axial tension. The springs are assumed to remain vertical, but they are able to slide freely in the $\tilde{x}$-direction.

Since the membrane is permeable, the flow field at very small scales near individual pores in the membrane is complex, and can lead to an effective slip velocity [34]. Provided the permeability is sufficiently weak, however (with pore dimensions sufficiently small and pore density sufficiently low), the slip velocity is small and the no-slip boundary condition can be applied: for full details see [16]. Thus the tangential component of the fluid velocity equals that of the membrane, and the normal component satisfies Starling's law, so that

$$\tilde{\mathbf{u}} = \frac{(-1, -\tilde{h}_x)}{(1+\tilde{h}_x^2)^{1/2}} + \epsilon^2(\tilde{p} - \tilde{\Pi})\mathbf{m} \qquad \text{on} \qquad \tilde{y} = \tilde{h}. \tag{6}$$

Here $\tilde{\Pi} = \Pi^* H^*/\mu U^*$ measures the strength of osmotic pressure to viscous pressures, and $\epsilon^2 = K^*\mu\,/H^*$ is a dimensionless permeability parameter, roughly proportional to the ratio of a typical pore width to the channel width. It is assumed that $\tilde{p}_b^* - \Pi^* > 0$, since otherwise the bubble would not propagate forwards.

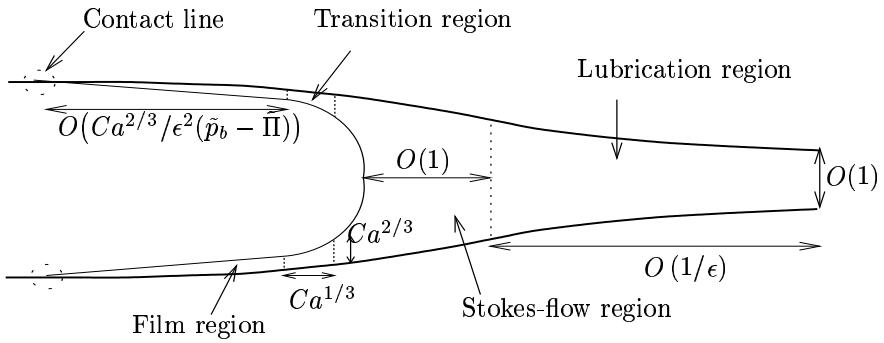

Figure 5: Asymptotic regions

As the bubble advances along the channel, it deposits a film on the channel membrane that drains through the membrane at a rate controlled by the membrane's permeability. This draining will result in a receding contact line at the end of the film. The details of the flow near the contact line are not of significance to the overall dynamics, so we simply set the slope as the fluid meets the membrane to some arbitrary value,

$$\tilde{h}_{\tilde{x}} - \tilde{f}_{\tilde{x}} = \tilde{\alpha} \qquad \text{where} \qquad \tilde{h} = \tilde{f}. \tag{7}$$

The flow within the channel is assumed to be symmetric about $\tilde{y} = 0$, therefore

$$\tilde{u}_{\tilde{y}} = \tilde{v} = 0 \qquad \text{on} \qquad \tilde{y} = 0. \tag{8}$$

Also, in order to avoid a singularity in the membrane curvature, the meniscus must be vertical at the bubble tip, and it is assumed that the membrane adopts a flat profile far ahead of the bubble, so

$$\lim_{\tilde{x}\to\infty} \tilde{h} = \tilde{h}_\infty. \tag{9}$$

where $\tilde{h}_\infty$ is a constant. Below we seek a solution of eqns (2)–(9) giving $\tilde{p}_b$ as a function of Ca, $\tilde{T}$, $\tilde{E}$, $\tilde{\Pi}$ and ϵ.

2.2 Asymptotic analysis

In order to solve this problem, we divide the solution domain into multiple regions and seek an asymptotic solution for slow bubble speeds ($Ca \ll 1$) and weak membrane permeability ($\epsilon \ll 1$). The appropriate limit for this solution is

$$\epsilon \ll Ca \ll 1. \tag{10}$$

We find that five regions are required by this approach, as sketched in Figure 5. Starting from the left, the first region is that around the receding contact line, where the last of the fluid that is left on the channel membrane

by the advancing meniscus leaves the channel. The adjacent *film region* is fluid deposited behind the bubble tip as it passes along the channel. This film is completely passive and is thin compared to the channel width; the film rests on the membrane and is gradually forced through it by the bubble and osmotic pressures. The *Stokes-flow region* occupies the space around the front of the meniscus. At low bubble speeds ($Ca \ll 1$), capillary forces dominate viscous forces, so the meniscus forms a surface of constant curvature, in this case a semi-circular cap. This region has an $O(1)$ aspect ratio, and the flow here is a fully two-dimensional Stokes flow. The *transition region* connects the film region and the Stokes-flow region. At leading order it has the same structure as the transition region described by Bretherton [3]. Across this region the fluid pressure falls from near $\tilde{p}_b$ (in the film region) to roughly $\tilde{p}_b - h_0/Ca$ (in the Stokes flow region), where h_0 is the channel width at the bubble tip. Viscous stresses balance the pressure drop across the transition region over a lengthscale $O(h_0 Ca^{1/3})$, and the film thickness in the transition region is $O(h_0 Ca^{2/3})$ [3]. The flux through this region is also $O(h_0 Ca^{2/3})$. Thus provided $h_0 = O(1)$, to leading order in Ca negligible fluid leaks past the meniscus. The *lubrication region* starts beyond the Stokes-flow region and extends far ahead of it. The length of the region is governed by the slow rate at which fluid can leave the channel through the weakly permeable membranes. This region needs to be long ($O(1/\epsilon)$), in order to allow all the fluid to escape. This low aspect ratio allows us to use lubrication theory, converting the two-dimensional Stokes flow equations into one-dimensional equations. This region provides the dominant contribution to the bubble pressure and is described in detail below. We will return to the remaining regions in Section 4.

2.3 The lubrication region

In the long lubrication region ahead of the bubble the majority of the oncoming plug flow (in the meniscus reference frame) escapes through the permeable membranes of the channel. We describe this by introducing rescaled variables

$$x = \epsilon\tilde{x}, \quad y = \tilde{y}, \quad h = \tilde{h}, \quad u = \tilde{u}, \quad v = \tilde{v}/\epsilon, \quad p = \epsilon\tilde{p}, \quad \Pi = \epsilon\tilde{\Pi}.$$

Then, with error $O(\epsilon^2)$, the governing equations become

$$u_x + v_y = 0, \quad p_x = \frac{\partial^2 u}{\partial y^2}, \quad p_y = 0, \tag{11}$$

$$p = E(h-1) - T\frac{d^2 h}{dx^2} \qquad \text{at} \qquad y = h, \tag{12}$$

where

$$T = \epsilon^3\tilde{T} = T^*\frac{1}{U^*}\left(\frac{\mu K^{*3}}{H^{*3}}\right)^{1/2}, \quad E = \epsilon\tilde{E} = E^*\frac{H^*}{U^*}\left(\frac{K^* H^*}{\mu}\right)^{1/2},$$

with

$$u = -1, \quad v = -\frac{dh}{dx} + p - \Pi \qquad \text{at} \qquad y = h, \tag{13}$$

$$u_y = 0, \quad v = 0 \qquad \text{at} \qquad y = 0 \tag{14}$$

and

$$\lim_{x \to \infty} h = h_\infty. \tag{15}$$

Integration of the continuity equation (see eqn (11)) across the channel from the centreline to the membran,e and incorporation of the boundary conditions eqns (13) and (14), yields

$$\frac{dQ}{dx} = \Pi - p \tag{16}$$

where

$$Q(x) = \int_0^{h(x)} u(x,y)dy$$

is the horizontal volume flux of fluid. The axial velocity is readily shown to be

$$u = \frac{1}{2}\frac{dp}{dx}(y^2 - h^2) - 1.$$

This can be integrated across the channel to give

$$Q(x) = -\frac{h^3}{3}\frac{dp}{dx} - h. \tag{17}$$

Equations (12), (16) and (17) form a closed system of ODEs for the horizontal flux, $Q(x)$, the pressure, $p(x)$, and the membrane position, $h(x)$.

The corresponding boundary conditions are determined as follows. In the far field downstream of the bubble, the fluid pressure is balanced solely by the elasticity of the membranes, so as $x \to \infty$, $h \to h_\infty$, $p \to E(h_\infty - 1)$ and $Q \to -h_\infty$. However from eqn (16), $p \to \Pi$, giving

$$h \to h_\infty = 1 + \frac{\Pi}{E} \qquad (x \to \infty). \tag{18}$$

As indicated above, the flux leaving the Stokes region around the bubble is $O(h_0 Ca^{2/3})$, where $h_0 \equiv h(0)$. Since we are making an asymptotic approximation for small Ca, this flux is, to leading order, zero. Since the flow is steady and the Stokes region is too short for any significant amount of fluid to leak through the membranes (see Section 4.1 below), the flux leaving the lubrication region must also be zero to leading order, i.e.

$$Q(0) = 0. \tag{19}$$

When the channel is very compliant, however ($E \ll 1$), the flux past the bubble tip can be significant, since $h(0)$ becomes large. We return to this possibility in Section 3.3 below.

The tension in the membrane requires the membrane displacement and slope to be everywhere continuous. The Stokes region is short and therefore the membrane displacement and slope do not change at leading order across it. The film deposited by the moving meniscus is passive, so the pressure at the membrane $p = p_b$ in $x \leq 0$. Equation (12) then gives

$$h(x) = 1 + \frac{p_b}{E} + A \exp\left(\sqrt{\frac{E}{T}} x\right) \qquad (x \leq 0)$$

for some constant A. Applying continuity of the membrane displacement and slope across the short inner regions yields

$$h(0) = 1 + \frac{p_b}{E} + \sqrt{\frac{T}{E}} \frac{dh}{dx}(0). \tag{20}$$

There are then three contributions to the bubble pressure,

$$p_b = p_t + p_s + p_l,$$

where p_t is the capillary pressure drop across the transition region, p_s is the viscous pressure drop across the Stokes region and $p_l = p(0)$ is the pressure drop across the lubrication region. In the current pressure scaling, these pressures are of the following order:

$$p_t \sim O\left(\frac{\epsilon}{Ca}\right), \quad p_s \sim O(\epsilon), \quad p_l \sim O(1).$$

Therefore, in the chosen limit $\epsilon \ll Ca \ll 1$, the bubble pressure is

$$p_b = p_l + O\left(\frac{\epsilon}{Ca}\right).$$

Thus the leading-order boundary condition on the membrane shape, eqn (20), becomes

$$h(0) = 1 + \frac{p(0)}{E} + \sqrt{\frac{T}{E}} \frac{dh}{dx}(0). \tag{21}$$

The full problem is therefore given by eqns (12, 16, 17), subject to (17, 18, 21). We seek p_l and the membrane shape $h(x)$ in terms of E, T and Π.

3 Lubrication region

We present results for the lubrication region by first considering the simplest case of purely rigid walls, before reintroducing the effects of springs and membrane tension.

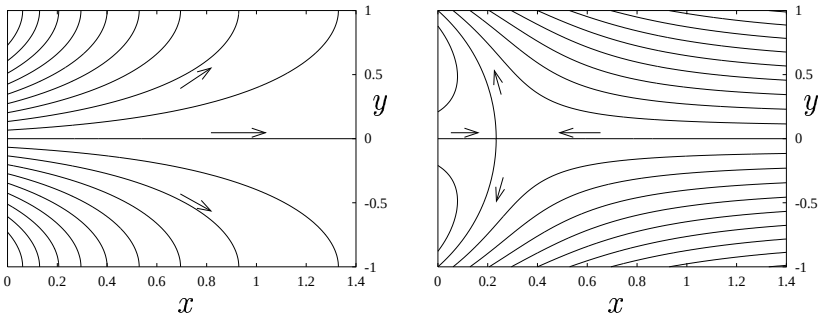

Figure 6: Streamlines in the channel wall reference frame (left) and the bubble-tip reference frame (right) with rigid walls, with streamline spacing of 0.1. Arrows indicate the direction of the flow.

3.1 Rigid walls

The rigid-walled case can be viewed as the limit of large stiffness ($E \to \infty$), for which $h \approx 1$. This immediately eliminates the membrane shape boundary condition eqn (21) and the membrane force balance condition eqn (12), yielding

$$Q(x) = -\frac{1}{3}\frac{dp}{dx} - 1, \qquad \frac{dQ}{dx} = \Pi - p, \tag{22}$$

along with the boundary conditions $Q(0) = 0$ and $Q \to -1$ as $x \to \infty$. These are easily solved to give

$$p(x) = \Pi + \sqrt{3}e^{-\sqrt{3}x}, \qquad Q(x) = e^{-\sqrt{3}x} - 1. \tag{23}$$

Thus the bubble pressure $p_b \approx p_l = \Pi + \sqrt{3}$. In dimensional terms, this is

$$p_b^* \approx p_l^* = \Pi^* + U^*\sqrt{\frac{3\mu}{K^* H^*}}. \tag{24}$$

Thus the bubble pressure rises linearly with the bubble speed, and the osmotic pressure appears additively. This is to be expected in this trivial case since without any mechanical pressure induced by membrane deformation, the osmotic pressure simply acts to elevate the effective interstitial pressure outside the channel.

The simple form of these solutions allows the calculation of the streamfunction ψ, where $(u, v) = (\psi_y, -\psi_x)$. In the frame of the bubble tip,

$$\psi(x, y) = \frac{y}{2}(3 - y^2)e^{-\sqrt{3}x} - y; \tag{25}$$

in the frame of the channel walls the streamfunction is eqn (25) without the $-y$ term. These streamfunctions are plotted in Figure 6. In the wall

reference frame, the meniscus advances and pushes the fluid out through the walls in front of it. The situation in the bubble-tip reference frame is more complex. Here, the basic downstream flow is that of an oncoming plug flow. This is pushed out of the walls by the pressure that increases towards the meniscus. This induces two counter-rotating vortices ahead of the meniscus. Lubrication theory is unable to resolve these vortices fully, but two-dimensional calculations are able to show how the streamlines within the stagnation-point streamline are closed near the meniscus; for details see [16].

3.2 The effect of membrane elasticity

We now introduce membrane deformation, controlled by springs, but suppose the membrane tension, T, is zero in eqn (12). A combination of the mass conservation equation (16) and the flux equation (17) with this simplified membrane force balance equation yields

$$\frac{E}{3}\frac{d}{dx}\left(h^3\frac{dh}{dx}\right) + \frac{dh}{dx} - Eh = -(\Pi + E). \tag{26}$$

Substitution of the simplified expression for the pressure from the membrane equation into the zero-flux boundary condition eqn (19) yields the condition

$$Eh^2(0)\frac{dh}{dx}(0) = -3. \tag{27}$$

The membrane slope continuity boundary condition eqn (21) is redundant in the absence of tension, and so eqns (26), (27) and the downstream boundary condition (18) completely specify this problem. It is readily solved with a shooting method, starting from an eigensolution of the linearized problem at large x and integrating back towards the bubble tip.

We first examine the bubble pressure as a function of spring stiffness E, assuming $\Pi = 0$. Figure 7 illustrates this relationship, with the value for the rigid wall on the same graph for comparison. Also shown is the membrane separation at the bubble tip, $h(0)$, as a function of E. These results show how the bubble pressure required to open the channel increases as the walls of the channel stiffen, and the bubble pressure increases with E towards its asymptotic rigid-walled limit. The membrane separation falls monotonically as E increases. As with the rigid-walled case, it is instructive to examine the streamlines in this regime. We consider two examples, one of low compliance ($E = 3$, Figure 8) and one of high compliance ($E = 0.1$, Figure 9). In the former case, the channel behaves similarly to the rigid-walled case (Figure 6), and the membrane shape follows the exponential pressure distribution. The situation in the high compliance case is strikingly different. The membrane deforms substantially over a large distance ahead of the bubble tip, and a large volume of fluid is pushed ahead of the advancing

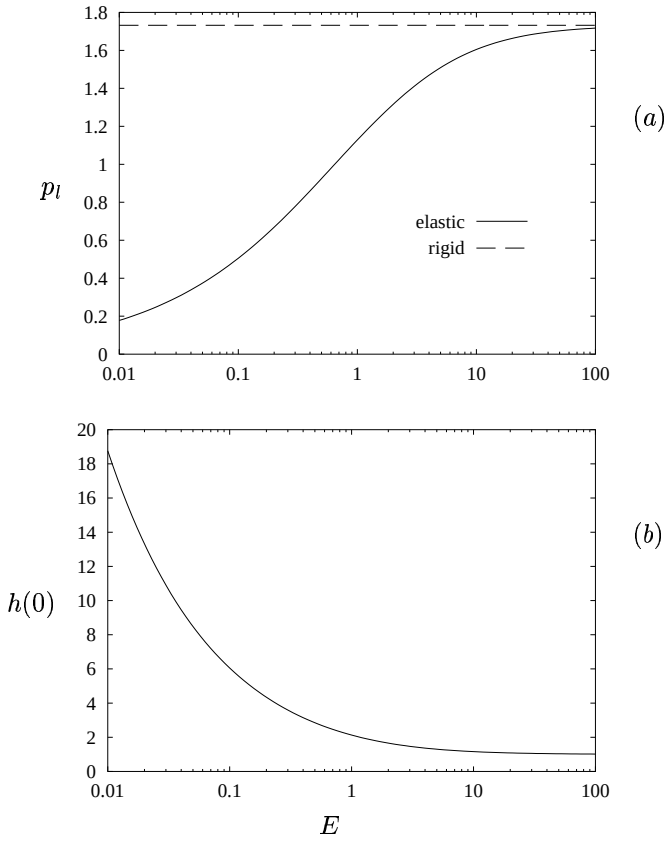

Figure 7: The leading-order approximation to (a) the bubble pressure, p_l, and (b) the membrane separation at the bubble tip, $h(0)$, as functions of the stiffness parameter, E.

meniscus. We therefore call this 'pushing' behaviour, similar to the pushing mode seen in the impermeable problem [8]. The streamlines in the bubble-tip reference frame exhibit long counter-rotating vortices, indicating that the majority of the fluid pushed along by the meniscus is trapped ahead of it.

The high compliance limit ($E \ll 1$) is amenable to asymptotic analysis, given in Appendix A. This yields an approximation to p_l,

$$p_l \approx 12^{\frac{1}{4}} E^{\frac{1}{2}} - \tfrac{19}{14} E + O(E^{\frac{3}{2}}). \tag{28}$$

The success of this approximation can be seen in Figure 10, which shows that eqn (28) is accurate even for quite large values of E. In terms of dimensional variables, the scaling $p_l \propto E^{1/2}$ implies that $p_b^* \propto U^{*1/2}$, so that the bubble

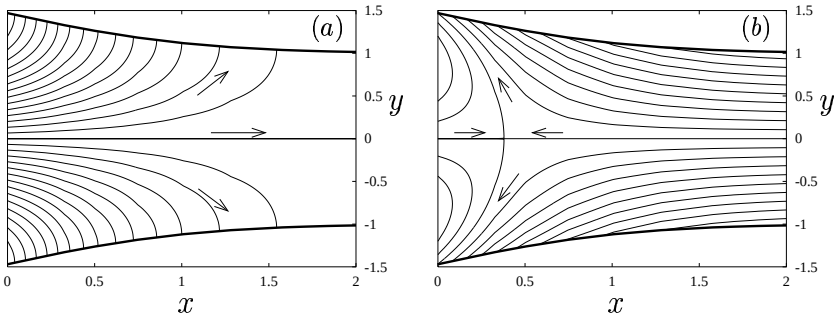

Figure 8: Streamlines in the channel wall reference frame (a) and the bubble tip reference frame (b) with low compliance walls, $E = 3$, and streamline spacing of 0.1.

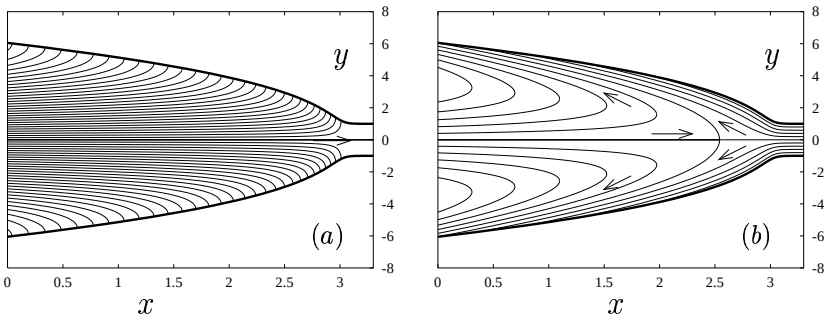

Figure 9: Streamlines in the channel wall reference frame (a) and bubble tip reference frame (b) with high compliance walls, $E = 0.1$ and streamline spacing of 0.2.

pressure increases monotonically but nonlinearly with bubble speed for very compliant channels.

3.3 Leakage past the bubble tip

The great width of the channel at the bubble tip in the pushing mode admits the possibility that the flux condition $Q(0) = 0$ is no longer valid. As demonstrated in Section 4 below, the flux past the bubble tip is $-\alpha h(0) Ca^{2/3}$ where $\alpha \approx 1.34$. The membrane displacement at the bubble tip $h(0) = O(E^{-1/2})$ for $E \ll 1$ (Appendix A). If $E^{1/2} \sim Ca^{2/3}$ the flux will no longer be negligible, and the bubble-tip flux condition must be modified from eqn (19) to

$$Q(0) = -\alpha h(0) Ca^{2/3}. \tag{29}$$

It is fortunate that a small modification to the pushing-mode asymptotics of Appendix A allows the capture of this regime. Since the flux falls towards

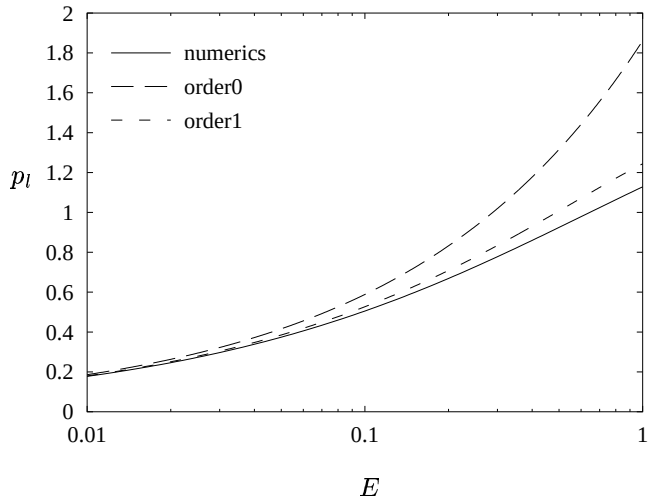

Figure 10: A comparison of the bubble pressure, p_l, from the numerical results with the bubble pressure from the pushing mode asymptotics as a function of the membrane stiffness parameter, E. One (order0) and two (order1) terms in eqn (28) are shown.

its downstream limit continuously in the pushing mode, one can select a point at which this boundary condition is satisfied, and then take this point to be the bubble tip for the modified problem. We thus obtain from eqn (29) and Appendix A

$$\frac{3^{5/3}}{4}(L-D)^{4/3} + \alpha 3^{2/3}(L-D)^{1/3}E^{-\frac{1}{2}}Ca^{2/3} - 1 = 0. \tag{30}$$

where $D/E^{1/2}$ is the bubble tip location and $L/E^{1/2}$ the length of the inflated region of the channel ahead of the meniscus. The new solution is simply the pushing mode solution displaced by $-D/E^{1/2}$ along the x-axis.

The leading-order bubble pressure from the pushing-mode asymptotics is (from eqn (56) below)

$$p_l \approx E^{\frac{1}{2}}\left[9\,(L-D)\right]^{\frac{1}{3}}, \tag{31}$$

which may be used to eliminate $L-D$ in eqn (30). This gives

$$\frac{p_l^4}{12E^2} + \alpha\frac{Ca^{2/3}}{E}p_l = 1. \tag{32}$$

It is useful at this point to rescale the variables, since our interest is in the bubble pressure as a function of Ca, so it is undesirable to have the pressure scaled on the bubble speed. Therefore, we adopt a pressure scale

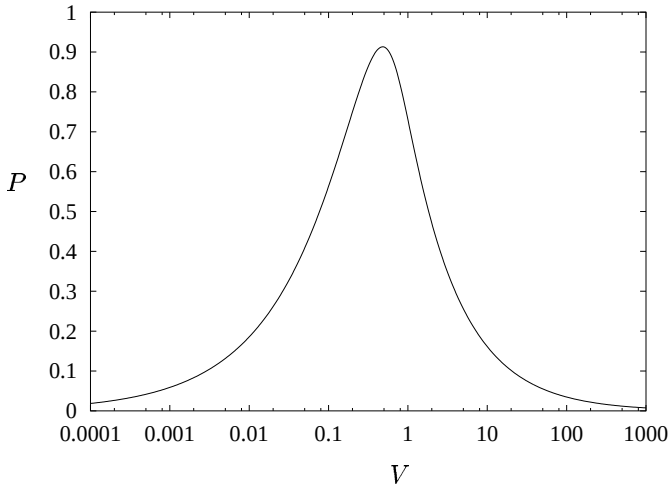

Figure 11: The rescaled bubble pressure P versus the rescaled bubble speed V.

purely based on material and geometric parameters, γ/H^*. The dependence of E on the bubble pressure is also undesirable, so the following parameter is introduced, following [8],

$$\Gamma = \frac{H^{*2}}{\gamma} E^* = Ca\tilde{E} = \frac{Ca}{\epsilon} E.$$

Making these changes in eqn (32) yields

$$\frac{\epsilon^2}{12Ca^2\Gamma^2}\hat{p}_l^4 + \alpha\frac{Ca^{2/3}}{\Gamma}\hat{p}_l = 1,$$

where $\hat{p}_l$ is the leading order bubble pressure scaled on γ/H^*. These terms balance when $Ca \sim (\epsilon\Gamma)^{3/7}$, $\hat{p}_l \sim (\Gamma^5/\epsilon^2)^{1/7}$, so the following scalings are made:

$$Ca = (\epsilon\Gamma)^{3/7} V, \qquad \hat{p}_l \sim \left(\Gamma^5/\epsilon^2\right)^{1/7} P.$$

This gives

$$\frac{1}{12}\frac{P^4}{V^2} + \alpha P V^{2/3} = 1. \tag{33}$$

This is easily solved numerically and the results may be seen in Figure 11. When V is small, the principal balance is between the P^4/V^2 and constant terms, so $P \sim V^{1/2}$, which is the usual scaling for the pushing mode in the present permeable-walled problem. However, when V is large, the principal

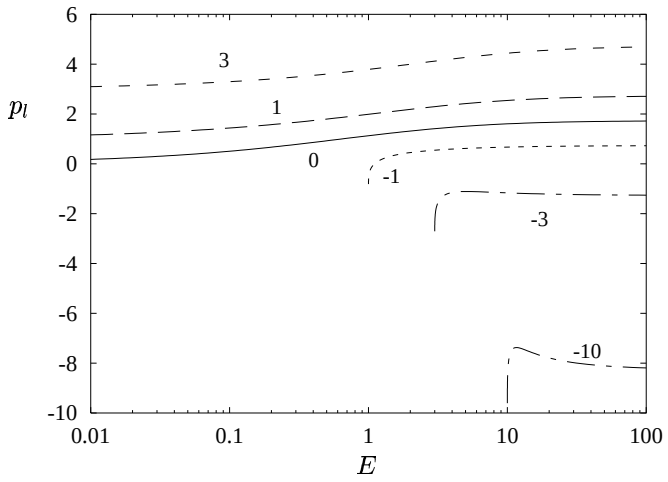

Figure 12: The leading order approximation to the bubble pressure, p_l, as a function of the elasticity parameter, E, for values of the osmotic pressure Π as shown.

balance is between the $PV^{2/3}$ and constant terms, so $P \sim V^{-2/3}$. This is the scaling seen on the left-hand, 'pushing' branch in [8] (see Figure 3). Thus, allowing leakage past the bubble tip connects the present permeable-walled problem to the impermeable-walled problem. The dimensional pressure and speed at which the turning point in the pressure-speed relation occurs is given approximately by

$$p_b^* = O\left(\left(\frac{\gamma^2 H^{*4} E^5}{\mu K^*}\right)^{\frac{1}{7}}\right), \qquad U^* = O\left(\left(\frac{\gamma^8 K^{*3} H^{*9} E^6}{\mu^{11}}\right)^{\frac{1}{14}}\right). \tag{34}$$

3.2 Non-zero osmotic pressure

We now introduce non-zero osmotic pressure and investigate the effect it has on the bubble pressure. Before that is done, however, it is important to note that for negative osmotic pressures solutions are unobtainable for high compliance channels. This is due to the fact that the downstream limit of the channel half-width is $1 + \Pi/E$. Therefore for $\Pi < -E$, the channel is completely collapsed and no bubble propagation is possible. With that caveat, solutions are produced by shooting in the same way as before and the results for a selection of osmotic pressures are shown in Figure 12. As one might expect, positive osmotic pressures have much the same effect on this elastic-walled problem as they do on the rigid-walled problem: they add to the bubble pressure required to open the channel at a given speed. Negative osmotic pressures act similarly for low compliance channels.

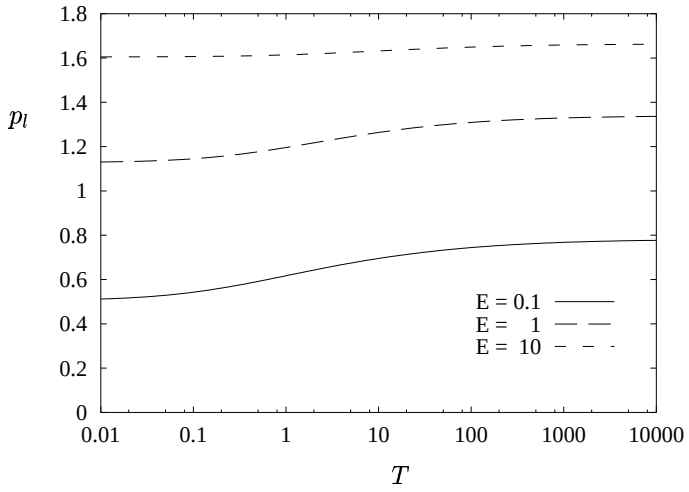

Figure 13: The leading order approximation to the bubble pressure, p_l, as a function of the membrane tension parameter, T, for various values of the membrane elasticity parameter, E.

As the compliance increases (E decreases), however, negative osmotic pressures have a profoundly different effect. As E approaches $-\Pi$, the bubble pressure drops rapidly towards Π. This is due to the channel approaching complete collapse as $E \searrow -\Pi$; very little pressure difference across the channel walls is then required to drive the small quantity of fluid out of the channel. For very low Π there is even a non-monotonic p_l-versus-E relationship. It should however be noted that these surprising effects are dependent on our extremely simple model of the membrane mechanics. If a more realistic, non-linear wall law were adopted, some of the more striking aspects of this behaviour would most likely disappear. We do not pursue that possibility here.

3.3 The effect of membrane tension

Reintroducing tension, the problem under consideration becomes the complete problem described in Section 2.3. A numerical solution of the full equations was obtained in this case by discretizing the governing ODEs and solving the resulting algebraic equations using Newton's method. For simplicity we restrict consideration to $\Pi = 0$; results are summarized in Figure 13. As one would expect, increasing membrane tension increases the effort required to open the channel. However, the important feature of these results is that this trend is weak. The bubble pressure does not vary very much with membrane tension, particularly when the membrane has low compliance ($E > 1$).

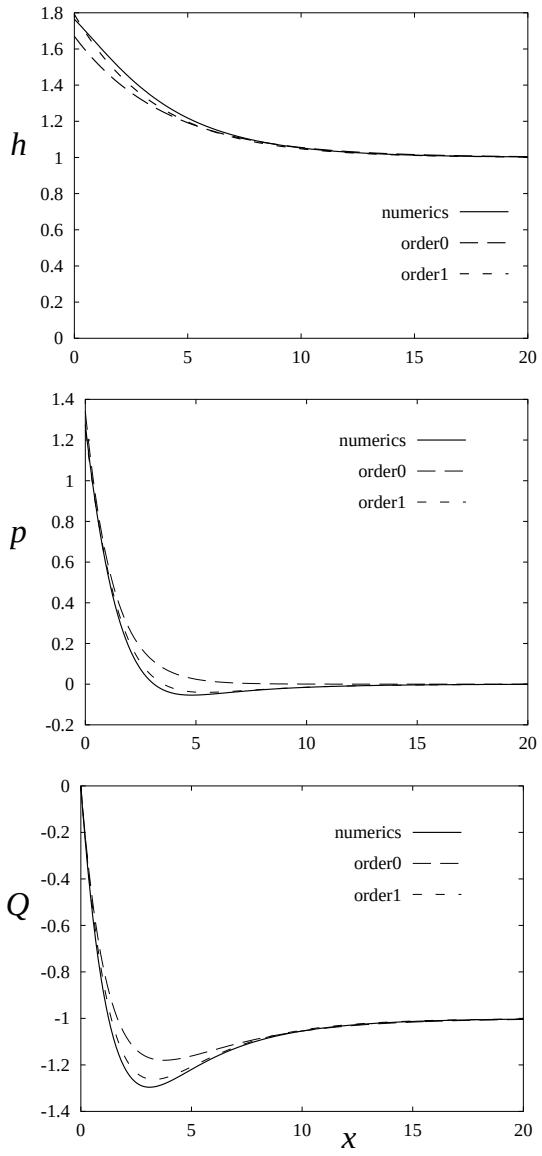

Figure 14: Solid lines show height, pressure and flux for $E = 1$ and $T = 16$. Dashed lines show the one-term (order0) and two-term (order1) asymptotic approximation (given in Appendix B) for $\delta = 0.25$.

When the membrane tension is large, a boundary-layer structure in the pressure and flux forms near the bubble tip, as can be seen in Figure 14. In this regime, the membrane displacement declines from its maximum at

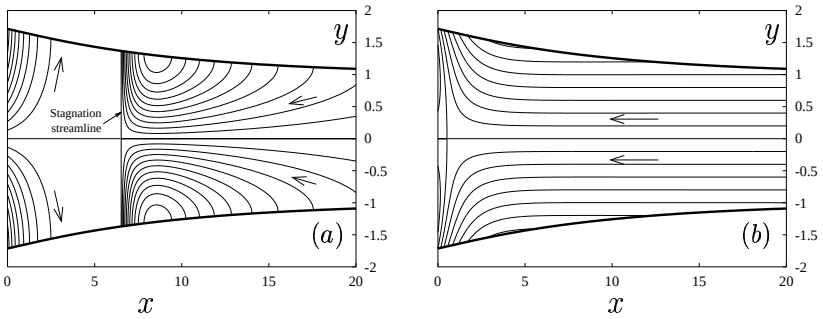

Figure 15: Streamlines in the channel wall reference frame (a) and the bubble-tip reference frame (b) for the peeling mode, $E = 1$ and $T = 100$. The streamline spacing in (a) is 0.2 to the left and 0.0002 to the right of the stagnation streamline; in (b) it is 0.2.

the bubble tip over a length-scale of $O(\sqrt{T/E})$. This slow decline is due to the balance between the elasticity and tension terms in eqn (12). The large tension ensures that the membrane shape cannot vary over short distances. However, the pressure and volume flux exhibit a boundary layer of $O(1)$ thickness near $x = 0$. The streamlines in Figure 15 illustrate how this occurs. The meniscus forces the liquid out of the channel over an $O(1)$ length, as in Figure 6. However, due to the high membrane tension the channel wall cannot deform over this short length. Therefore, it relaxes to match the downstream boundary condition over a longer length-scale. Also, since the membrane is curved upwards in this region, the pressure within the channel is negative. This negative pressure induces a weak inflow through the permeable walls. Thus in this regime there exists a region of inflow in addition to the usual outflow region. This can also be seen in Figure 14, where the flux drops below the downstream limit of -1 before climbing to match the bubble-tip flux boundary condition.

This structure is amenable to analysis by means of matched asymptotics with a small parameter $\delta = \sqrt{E/T}$. Details of this analysis can be found in Appendix B. It yields a composite approximation for h, p and Q, valid across the entire domain, and allows the calculation of the bubble pressure,

$$p_l \approx \Pi + \sqrt{\frac{3}{H_0}} + \delta\left[\frac{H_1}{2}\sqrt{\frac{3}{{H_0}^3}} + \frac{3H_D}{4}\right] - \delta G_0, \tag{35}$$

where $H_0 \equiv h_0$, G_0, H_1 and H_D are functions of E (and, if appropriate, Π) given in Appendix B. A comparison of this result with the numerical results is presented in Figure 16. It is clear from this graph that the $O(\delta)$ asymptotics are reasonably accurate even at low membrane tensions. This

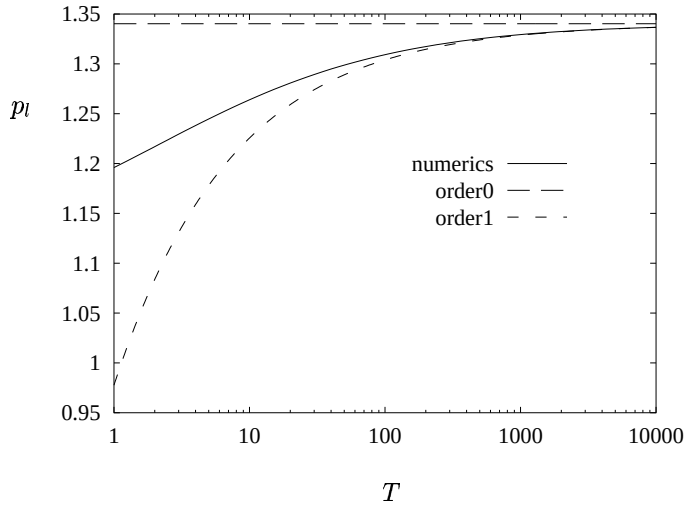

Figure 16: A comparison of the numerical results with the peeling mode asymptotics. p_l is plotted as a function of the membrane tension parameter, T, for $E = 1$. One (order0) and two (order1) terms in eqn (35) are shown.

result is reinforced by Figure 14, where the spatial variation of the composite approximation and numerical results are presented. Even though δ is relatively large, the asymptotics are still respectably accurate.

4 Stokes, transition and film regions

Having determined the structure of the flow in the lubrication region ahead of the bubble, we now return to the Stokes, transition and film regions which were introduced in Section 2 (and are illustrated in Figure 5). Under normal conditions they do not contribute to the leading-order bubble pressure, yet it is important to have a clear picture of their structure.

4.1 Stokes region

The Stokes region is the zone near and around the bubble tip having $O(1)$ aspect ratio, in which the flow is inherently two-dimensional. The assumption of low capillary number implies that capillary forces dominate viscous forces in this region, so that the meniscus has constant curvature to leading order, forming a semi-circular cap that almost fills the channel, joining onto thin films on each membrane of thickness $O(Ca^{2/3})$ (assuming $h(0) = O(1)$). The viscous pressure drop across this region is $O(1)$. This is much smaller than the $O(1/\epsilon)$ pressure drop across the lubrication region,

and the $O(1/Ca)$ capillary pressure drop across the meniscus, so there is no need to compute the details of the flow. The membrane is approximately flat over the Stokes region provided E and T are both sufficiently large: in the pushing regime, this condition becomes $\epsilon \ll E^{1/2} \ll 1$; in the peeling regime, the large tension ensures that the membrane remains flat for $E = O(1)$, [16].

In order to impose the flux boundary condition eqn (19) or eqn (29) on the upstream end of the lubrication region, it is important to estimate the flux that crosses the membrane in the Stokes region. This is done by observing that the pressure within this region is $O(1/\epsilon)$ and its length is $O(1)$. Therefore from eqn (6) the flux crossing the membrane in the Stokes region will be $O(\epsilon)$. Thus, the loss of fluid through the membranes in this region may safely be neglected in determining the flux leaving the lubrication region, since the flux through the transition region is $O(Ca^{2/3}) \gg O(\epsilon)$ (from eqn (10)).

4.2 Transition, film and contact-line regions

These three regions encompass all of the thin film laid down by the advancing meniscus. Across the short transition region the fluid pressure changes by $O(1/Ca)$, from being equal to the bubble pressure in the film region to a lower capillary pressure in the Stokes region. In the film region the bulk of the fluid deposited by the transition region leaks out slowly through the membrane. The contact-line region at the end of the film is of particular interest since (as shown below) the contact line moves without causing a stress singularity, despite the imposition of the no-slip condition.

Since all three regions are slender, with aspect ratio δ, say, we can use lubrication theory to describe their structure. Defining $\tilde{t} = \tilde{h} - \tilde{f}$ to be the thickness of the film deposited on the membrane, the governing equations are

$$\nabla \cdot \tilde{\mathbf{u}} = 0, \quad \tilde{p}_{\tilde{x}} = \frac{\partial^2 \tilde{u}}{\partial \tilde{y}^2}, \quad \tilde{p}_{\tilde{y}} = 0,$$

subject to

$$\tilde{p} = \tilde{p}_b - \frac{1}{Ca}\frac{d^2\tilde{t}}{d\tilde{x}^2}, \tag{36}$$

$$\tilde{u}_{\tilde{y}} = 0, \quad \tilde{v} = \tilde{u}(\tilde{h} - \tilde{t})_{\tilde{x}} \qquad \text{on} \qquad \tilde{y} = \tilde{h} - \tilde{t}, \tag{37}$$

$$\tilde{u} = -1, \quad \tilde{v} = \epsilon^2(\tilde{p} - \tilde{\Pi}) \qquad \text{on} \qquad \tilde{y} = \tilde{h}, \tag{38}$$

with error $O(\delta^2)$. Provided $T \gg \epsilon^2 E^{1/2} Ca^{1/3}$, the flow induced by membrane curvature is negligible in eqn (36), [16]. As is usual with the lubrication approximation, the pressure within the fluid is now purely a function of $\tilde{x}$.

Thus, the $\tilde{x}$ component of the momentum equation can be integrated using the boundary conditions on $\tilde{u}$ to give a horizontal volume flux,

$$\tilde{Q}(\tilde{x}) = -\frac{\tilde{t}^3}{3}\frac{d\tilde{p}}{d\tilde{x}} - \tilde{t}. \tag{39}$$

The mass conservation equation is integrated with respect to $\tilde{y}$ and the $\tilde{v}$ boundary conditions imposed, yielding

$$\frac{d\tilde{Q}}{d\tilde{x}} = \epsilon^2(\tilde{\Pi} - \tilde{p}). \tag{40}$$

Since there is no spanwise variation in the pressure, eqn (36) describes the pressure throughout the film. Substituting this and eqn (39) into eqn (40) yields

$$\frac{1}{Ca}\frac{d}{d\tilde{x}}\left(\frac{\tilde{t}^3}{3}\frac{d^3\tilde{t}}{d\tilde{x}^3}\right) = \frac{d\tilde{t}}{d\tilde{x}} + \epsilon^2\left(\frac{1}{Ca}\frac{d^2\tilde{t}}{d\tilde{x}^2} + \tilde{\Pi} - \tilde{p}_b\right). \tag{41}$$

This may be integrated with respect to $\tilde{x}$, yielding

$$\frac{\tilde{t}^3}{3Ca}\frac{d^3\tilde{t}}{d\tilde{x}^3} = \tilde{t} + \frac{\epsilon^2}{Ca}\frac{d\tilde{t}}{d\tilde{x}} + \epsilon(\Pi - p_b)\tilde{x} + \tilde{q}_0, \tag{42}$$

where $\tilde{q}_0$ is some constant to be determined by boundary conditions. The terms in this equation are all fluxes with different sources. They are, respectively, the flux driven by the capillary pressure, the flux due to the moving wall, the capillary-pressure-driven transmural flux, the bubble- and osmotic-pressure-driven transmural flux and a constant flux required to match boundary conditions. The three regions are governed by different dominant balances between these terms.

4.2.1 Transition region

The transition region connects the film and the meniscus, near $\tilde{x} = -h(0)$, and is dominated by an abrupt change in pressure due to an abrupt change in interfacial curvature. From Landau & Levich [22] and Bretherton [3], we know that for $Ca \ll 1$ the region has a length of $O(Ca^{1/3})$ and a film thickness of $O(Ca^{2/3})$, so we set

$$\tilde{x} = h(0)(Ca^{1/3}x - 1), \quad \tilde{t} = h(0)Ca^{2/3}t.$$

Under these scalings, eqn (42) becomes, at leading order,

$$\frac{t^3}{3}\frac{d^3t}{dx^3} = t + q_0 \quad \text{where} \quad q_0 = \frac{\tilde{q}_0 Ca^{-2/3}}{h(0)}. \tag{43}$$

The region is short enough for negligible fluid to leak through the membrane. In order to match to the semi-circular meniscus in the Stokes region, we have

$$\lim_{x\to\infty}\frac{d^2t}{dx^2} = 1. \tag{44}$$

To match to the film region,

$$\lim_{x \to -\infty} t = -q_0. \tag{45}$$

This system of equations has a unique solution, up to translation in x [3], from which we find that $-q_0 \approx 1.337$. In the original non-dimensional variables, the film thickness where the transition and film regions overlap is approximately $1.337\,h(0)Ca^{2/3}$, which is also the horizontal flux passing through the transition region. Provided $h(0) = O(1)$, this flux is negligible compared to that leaving through the membrane in the lubrication region ahead of the bubble. The possibility that $h(0)$ is large and that this flux is significant was considered in Section 3.3.

4.2.2 Film region

The film deposited immediately behind the bubble leaks out steadily through the membrane. The dominant balance of terms is captured by rescaling using

$$\tilde{x} = h(0)\left(\frac{Ca^{2/3}}{\epsilon(p_b - \Pi)}x - 1\right), \quad \tilde{t} = h(0)Ca^{2/3}t,$$

and eqn (42) becomes

$$\frac{\epsilon^3(p_b - \Pi)^3}{3Ca^{1/3}}\frac{t^3}{3}\frac{d^3t}{dx^3} = t + \frac{\epsilon^3(p_b - \Pi)}{Ca}\frac{dt}{dx} - x - \epsilon h(0)(\Pi - p_b) + q_0, \tag{46}$$

where q_0 is defined as in eqn (43). At leading order eqn (46) becomes

$$t = x - q_0. \tag{47}$$

Matching with the transition region we have $t(0) = -q_0 = 1.337$, and returning to the original variables this gives the film thickness as

$$\tilde{t} = \epsilon(p_b - \Pi)(\tilde{x} + h(0)) + 1.337h(0)Ca^{2/3}. \tag{48}$$

The film thickness declines linearly from the transition region, with slope $-\epsilon(p_b - \Pi)$.

4.2.3 Contact line region

The film must satisfy the imposed contact angle condition, eqn (7), at the contact line,

$$\frac{d\tilde{t}}{d\tilde{x}} = \tilde{\alpha} \qquad \text{where} \qquad \tilde{t} = 0. \tag{49}$$

Therefore, just before the film thickness falls to zero, another region is required to match to the prescribed contact angle. Here the dominant balance is the same as the film region, with the addition of the term due to

the capillary-pressure-driven transmural flux. To capture this balance, we rescale using

$$\tilde{x} = \frac{\epsilon^2}{Ca}x - h(0)\left(1 - q_0\frac{Ca^{2/3}}{\epsilon(p_b - \Pi)}\right), \quad \tilde{t} = \frac{\epsilon^3(p_b - \Pi)}{Ca}t.$$

Equation (42) then becomes

$$\frac{\epsilon^3(p_b - \Pi)^3}{3Ca}\frac{t^3}{3}\frac{d^3t}{dx^3} = t + \frac{dt}{dx} - x + q_0, \tag{50}$$

where all the constant terms have been absorbed into q_0. At leading order, (50) becomes

$$\frac{dt}{dx} = x - t - q_0.$$

The contact angle condition demands that

$$\frac{dt}{dx} = \alpha \qquad \text{where} \qquad t = 0, \qquad \alpha = \frac{1}{\epsilon(p_b - \Pi)}\tilde{\alpha}.$$

To match with the outer film region, we have $t \to x$ as $x \to \infty$. The solution in this region is therefore

$$t = (1 - \alpha)e^{\alpha - 1 - x} + x$$

and the contact line is located at $x = \alpha - 1$. Thus, the film thickness has a locally quadratic profile at the contact line, matching onto the linear outer region exponentially. In the special case $\alpha = 1$ the film thickness is linear right up to the contact line. The value of α is set by material properties. If disjoining pressures keep the lung walls wet, we take $\alpha = 0$, for example.

This region has no effect on the global behaviour of the system, since it does not affect the bubble pressure. It is still of particular interest, as it is a moving contact line with the no-slip condition yet it does not manifest the stress singularity usually seen in these problems. This is because the mechanism for moving the contact line is not one of dragging it across the surface. Instead, the fluid merely moves through the membrane, leaving a section of membrane dry which was previously wet. Similar behaviour was seen by Neogi & Miller [29] and Davis & Hocking [4, 5] in studies of contact lines advancing over permeable substrates.

5 Discussion

5.1 Pressure-speed relations

We have shown that for a bubble reopening a channel with flexible, permeable walls, the pressure required to move the bubble steadily at a dimensionless speed $Ca \ll 1$ is given approximately by the sum of the pressure

drop across the long lubrication region ahead of the bubble tip and the capillary pressure drop across the meniscus. These are the first two terms of an asymptotic expansion in ϵ and Ca. In the original non-dimensional variables (scaling pressures on $\mu U^*/H^*$) they are

$$\tilde{p}_b = \frac{1}{\epsilon} p_l(Ca, E, T) + \tilde{p}_t(Ca, E, T) + O(1),$$

where $\tilde{p}_t = 1/\{h_0(Ca, E, T)Ca\}$ and $h_0 \equiv h(0)$. The principal result of interest is how the bubble pressure varies with bubble speed. In order to do this, a scaling in which the non-dimensional pressure does not depend on the bubble speed is required. Thus, we rescale onto a capillary pressure scale, γ/H^* (as in [8]),

$$\hat{p}_b = \tilde{p}_b Ca = \frac{H^*}{\gamma} p_b^*.$$

Similarly, the wall parameters are rescaled to avoid their dependence on the bubble speed so, again following [8], we set

$$\Gamma = \frac{H^{*2}}{\gamma} E^* = Ca\tilde{E} = \frac{Ca}{\epsilon} E, \quad \eta = \frac{T^*}{\gamma} = Ca\tilde{T} = \frac{Ca}{\epsilon^3} T.$$

We can then write

$$\hat{p}_b\big(\Gamma, \eta, \epsilon; Ca\big) = \frac{1}{\epsilon} p_0\big(\epsilon\Gamma, \epsilon^3\eta; Ca\big) + p_1\big(\epsilon\Gamma, \epsilon^3\eta; Ca\big) + O(Ca). \tag{51}$$

where

$$p_0 = Ca\, p_l\left(Ca, \frac{\epsilon}{Ca}\Gamma, \frac{\epsilon^3}{Ca}\eta\right), \quad p_1 = 1\Big/h_0\left(Ca, \frac{\epsilon}{Ca}\Gamma, \frac{\epsilon^3}{Ca}\eta\right). \tag{52}$$

We first examine the spring-dominated case, where $T \ll 1$. Figure 17 is a graph of the leading-order bubble pressure as a function of capillary number, for various values of $\epsilon\Gamma$. For large stiffness, the wall is almost rigid and p_0 increases linearly with Ca, consistent with the result in Section 3.1. Reducing the stiffness Γ reduces the bubble pressure significantly. When the wall is floppy ($\epsilon\Gamma$ small), the system is in the pushing mode, and p_0 rises in proportion to $Ca^{1/2}$. The first correction to the bubble pressure is plotted in Figure 18. As expected, there is little variation in this correction when the wall is almost rigid, since the wall displacement at the bubble tip does not vary and this correction is simply the fixed pressure drop across a semi-circular meniscus in a rigid channel. When the walls are floppy however, the pushing mode dominates, so $h \sim E^{-1/2}$. Due to the dependence of E on Ca, this means that $p_1 \propto Ca^{-1/2}$.

Tension has a much weaker effect on the pressure-speed relation, as shown in Figure 19, since it causes only a modest increases in the reopening pressure. Since both T and E are inversely proportional to Ca, when Ca is

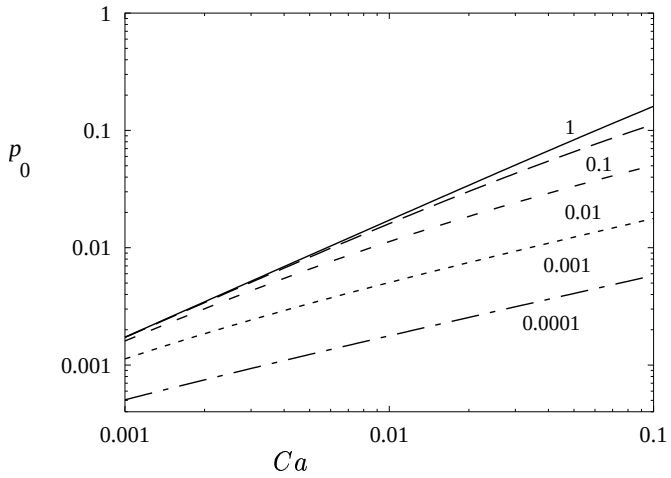

Figure 17: The leading order approximation to the bubble pressure, p_0, as a function of the capillary number, Ca, for the purely elastic-walled problem, with values of $\epsilon\Gamma$ as shown.

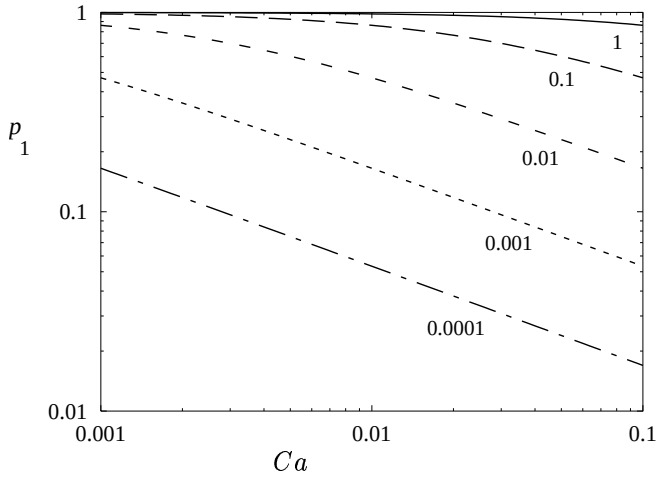

Figure 18: The first correction to the bubble pressure, p_1, as a function of the capillary number, Ca, for the purely elastic-walled problem, with values of $\epsilon\Gamma$ as shown.

varied the effect of elasticity therefore dominates. Figure 20 shows how wall tension has the effect of considerably reducing the elasticity-induced variation in the first correction. This is because wall tension prevents the wall from being displaced too much at the bubble tip, limiting variations in the

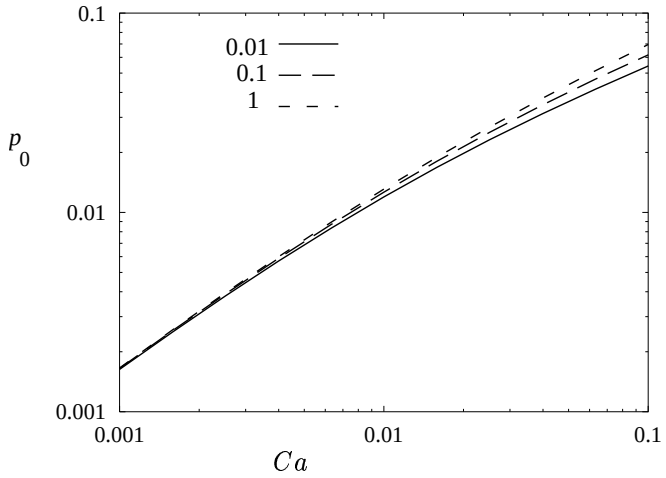

Figure 19: The leading order approximation to the bubble pressure, p_0, as a function of the capillary number, Ca, for the full problem, with $\epsilon\Gamma = 10^{-2}$ and values of $\epsilon^3\eta$ as shown.

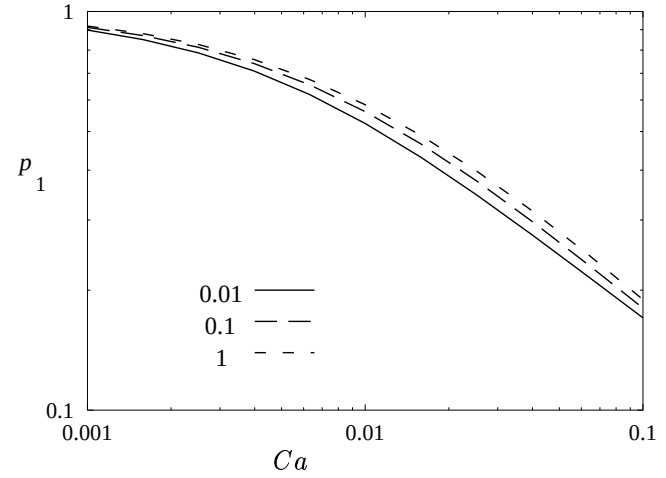

Figure 20: The first correction to the bubble pressure, p_1, as a function of the capillary number, Ca, for the full problem, with $\epsilon\Gamma = 10^{-2}$ and values of $\epsilon^3\eta$ as shown.

capillary pressure drop across the meniscus. Very large variations in tension are therefore required for it to have a significant effect on reopening.

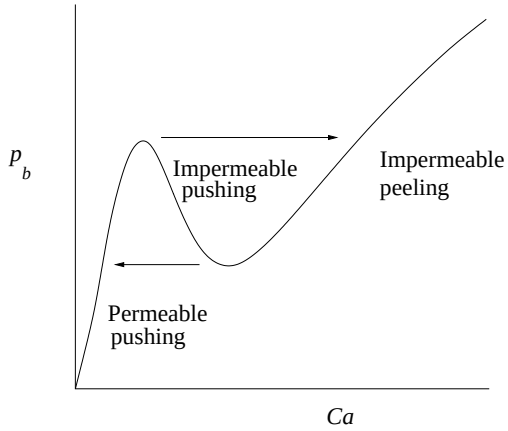

Figure 21: A schematic diagram of p_b versus Ca showing hysteresis between the permeable and impermeable solution branches.

5.2 Link with the impermeable problem

Increasing the bubble pressure and the reopening speed increases the channel width at the bubble tip, and hence the flux of liquid that escapes past the bubble into a film deposited on each membrane. As shown in Section 3.3, this flux cannot be neglected if E is low and the channel inflates sufficiently. Inclusion of this flux yields a pressure-speed relation that is non-monotonic, as illustrated in Figure 11 for low speeds and Figure 21 for a wider range of Ca. At large speeds, the effects of permeability become less significant and the channel behaves as if it were impermeable, and the system connects onto the impermeable 'pushing' branch identified by Gaver *et al.* [8]. As Figure 3 indicates, this branch in turn is connected to an impermeable 'peeling' branch, which we know from [16] to be stable to perturbations at fixed bubble pressure. We conclude that once p_b^* increases beyond the critical value given in eqn (34), the system will jump abruptly across to the peeling solution at that bubble pressure, as illustrated in Figure 21. Accounting for permeability therefore leads to hysteresis in the pressure-speed relation.

5.3 Application to lung airways

We can tentatively estimate the value of the model's parameters in the context of lung airways. Matsui *et al.* [25] give a value for the transepithelial osmotic permeability coefficient of 150–250 μm/s, from which we obtain the estimate $K^* \approx 10^{-11}$ cm^2/gm [16], which implies $\epsilon \approx 10^{-6}$ in a 1 mm radius airway filled with water. An alternative estimate of permeability is $K^* \approx R\alpha/\mu$, where R is the size of a pore between epithelial cells, α is the area fraction occupied by the pores and μ is the fluid viscosity. If $\alpha \approx 10^{-2}$

and $R \approx 1$nm then $\epsilon \approx 10^{-4}$ for a 1 mm airway. Despite the likelihood of significant variations between disease states, the assumption that ϵ is small is well justified. However, this very small value for ϵ implies that permeability effects manifest themselves over very long lengthscales, certainly extending over many airway generations. Future models should take proper account of the branching structure of multiple generations and of end effects in finite-length flow domains.

Perhaps more significantly, eqn (34) provides approximate upper bounds on the bubble pressure and bubble speed for which the effects of permeability are likely to be significant in a long compliant airway. They indicate that permeability matters only for very slowly propagating bubbles, and that under normal ventilatory conditions airways are likely to behave as if they were impermeable.

5.4 Summary

We have presented a model exploring the effects of weak wall permeability on lung airway reopening. At sufficiently low bubble pressures and low bubble propagation speeds, a bubble advancing in a permeable, deformable channel behaves like a piston, pushing fluid ahead of itself and outwards through the channel walls. The elevated channel pressure deforms the channel walls. High membrane tension can result in fluid being first sucked into the channel and later pushed out. Very compliant channels can become widely dilated as the bubble pressure is increased: in this case a significant flux of fluid past the bubble tip allows us to connect the solution to the 'pushing' mode identified in [8]. Fluid deposited on the channel wall in this case forms a finite-length film that terminates in a contact line that is not subject to the usual non-integrable stress singularity.

This study, in conjunction with other theoretical and experimental studies outlined in Section 1, helps to broaden our overall understanding of bubble propagation in flexible channels. The challenge now is to link these simplified physical and theoretical models with the reopening of real airways.

Acknowledgements

This work was undertaken while Mark Horsburgh was a Research Student in the Department of Applied Mathematics and Theoretical Physics, University of Cambridge, UK.

Appendix

(A) Pushing mode asymptotics

Here the asymptotics of the pushing mode are described for high compliance tubes, where $E \ll 1$, assuming the osmotic pressure is zero, and neglecting

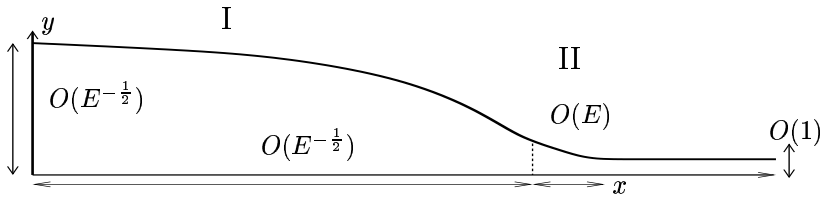

Figure 22: Asymptotic regions in the pushing mode. Region I is a long, fat plug of fluid being pushed in front of the meniscus. Region II is a short region in which the wall adjusts to its equilibrium value.

the effects of membrane tension. The governing equations are then

$$\frac{dQ}{dx} = -p, \quad Q = -\frac{h^3}{3}\frac{dp}{dx} - h, \quad p = E(h-1), \tag{53}$$

with $Q(0) = 0$ and $h \to 1$ as $x \to \infty$.

The solution domain is divided into two regions, as illustrated in Figure 22. Region I is the long, fat plug of fluid where the dominant balance is between the flux driven by pressure gradients and that driven by the moving walls. Region II is where the wall displacement adjusts over a very short length to the downstream boundary condition.

In Region I, the wall displacement and the horizontal length-scale are large. Therefore, the leading order balance is such that the pressure is approximately Eh. This, in conjuction with the zero-flux boundary condition (which requires that the two terms in the expression for the flux must balance), the mass conservation equation (53a), and the fact that $Q = O(1)$ from the far-field condition, implies that the wall displacement and horizontal lengths scale as $E^{-1/2}$. Thus the pressure scales with $E^{1/2}$. Thus we rescale the variables in Region I as

$$x = E^{-1/2}x_I, \quad h = E^{-1/2}h_I, \quad p = E^{1/2}p_I, \quad Q = Q_I. \tag{54}$$

The rescaled governing equations are then

$$\frac{dQ_I}{dx_I} = -p_I, \quad E^{1/2}Q_I = -\frac{h_I^3}{3}\frac{dp_I}{dx_I} - h_I, \quad p_I = h_I - E^{1/2} \tag{55}$$

with $Q_I(0) = 0$.

The dependent variables are expanded in a power series in $E^{1/2} \ll 1$, with $h_I = h_0 + E^{1/2}h_1 + Eh_2 + \ldots$ and so on. These power series are placed

in the governing equations and terms of the same order are matched. The resulting equations are then solved, which yields, with error $O(E)$,

$$h_I = [9(L-x_I)]^{\frac{1}{3}} + E^{\frac{1}{2}}\frac{3^{\frac{2}{3}}}{8}\left[(L-x_I)^{\frac{4}{3}} - 3L^{\frac{4}{3}} - \frac{L^2}{7}(L-x_I)^{-\frac{2}{3}}\right],$$

$$p_I = [9(L-x_I)]^{\frac{1}{3}} + E^{\frac{1}{2}}\frac{3^{\frac{2}{3}}}{8}\left[(L-x_I)^{\frac{4}{3}} - 3L^{\frac{4}{3}} - \frac{L^2}{7}(L-x_I)^{-\frac{2}{3}}\right] - E^{\frac{1}{2}}$$

and

$$Q_I = \frac{3^{\frac{5}{3}}}{4}\left[(L-x_I)^{\frac{4}{3}} - L^{\frac{4}{3}}\right] + E^{\frac{1}{2}}\left\{\left(1+\frac{3^{\frac{5}{3}}}{8}L^{\frac{4}{3}}\right)x_I + \frac{3^{\frac{5}{3}}}{56}\left[(L-x_I)^{\frac{7}{3}} - L^2(L-x_I)^{\frac{1}{3}}\right]\right\},$$

where L is some constant to be determined by matching.

The leading order pressure in Region I, expressed in the unscaled variables, is

$$p = \left[9E^2(E^{-\frac{1}{2}}L - x)\right]^{\frac{1}{3}}. \tag{56}$$

This approximation fails when $p = O(E)$, so this implies the need for another region (Region II in Figure 22) where $h = O(1)$ and $p = O(E)$ and where deviations in x from $E^{-\frac{1}{2}}L$ are $O(E)$. The mass conservation equation then implies that deviations in the flux must be $O(E^2)$. Thus, we adopt the following scalings

$$h = h_{II} + 1, \quad x = E^{-\frac{1}{2}}L + Ex_{II}, \quad p = Ep_{II}, \quad Q = E^2Q_{II} - 1, \tag{57}$$

which yield these governing equations

$$\frac{dQ_{II}}{dx_{II}} = -p_{II}, \quad E^2Q_{II} = \frac{(h_{II}+1)^3}{3}\frac{dp_{II}}{dx_{II}} - h_{II}, \quad p_{II} = h_{II}. \tag{58}$$

The dependent variables are expanded in a power series in E^2, so $h_{II} = h_0 + E^2h_1 + E^4h_2 + \ldots$ and so on. This yields the equation for the leading order wall displacement,

$$\frac{h_0^3}{3} + \frac{3h_0^2}{2} + 3h_0 + \ln h_0 = -3x_{II} + K \tag{59}$$

for some real constant K.

The leading order expression for the flux in Region I in terms of the Region-II variables is

$$E^2Q_{II} - 1 = \frac{3^{\frac{5}{3}}}{4}\left[E^2x_{II}^{\frac{4}{3}} - L^{\frac{4}{3}}\right]. \tag{60}$$

Matching the $O(1)$ terms in this equation yields $L = \left(2^6/3^5\right)^{\frac{1}{4}}$. Thus we have the expression for the leading order bubble pressure given in eqn (28).

(B) Peeling mode asymptotics

In this section, the details of the peeling mode asymptotics introduced in Section 3.5 are described. This regime can be described by matched asymptotics, with the solution domain divided into two regions. The inner region around the bubble tip has $O(1)$ length and is where the bulk of the change in the horizontal fluid flux occurs. The outer region has $O(\sqrt{T/E})$ length and is where the wall displacement relaxes to match the downstream boundary condition. Therefore,

$$\delta = \sqrt{E/T} \tag{61}$$

is adopted as the small parameter in the asymptotic expansion.

The inner region requires no rescaling, so the governing equations are

$$\delta^2 p = E[\delta^2(h-1) - h_{xx}], \quad Q_x = \Pi - p, \quad Q = -\frac{h^3}{3}p_x - h \tag{62}$$

with boundary conditions $Q(0) = 0$ and

$$h_x(0) = \delta\left(h(0) - 1 - \frac{p(0)}{E}\right). \tag{63}$$

Each of the dependent variables is expanded in a power series in δ, so $h = h_0 + \delta h_1 + \delta^2 h_2 + O(\delta^3)$, and so on. Substituting the power series into the governing equations yields long expressions (given in [16]) involving constants $H_0 = h_0$, H_1, H_2 and

$$H_D = H_0 - 1 - \frac{\Pi}{E} - \frac{1}{E}\sqrt{\frac{3}{H_0}}. \tag{64}$$

These constants must be determined by matching.

In the outer region the x coordinate requires rescaling, so a new variable is defined, $\xi = \delta x$. The governing equations in this region are then

$$p = E(h - 1 - h_{\xi\xi}), \quad \delta Q_\xi = \Pi - p, \quad Q = -\delta\frac{h^3}{3}p_\xi - h \tag{65}$$

where

$$\lim_{\xi\to\infty} h = 1 + \frac{\Pi}{E}. \tag{66}$$

Again, the dependent variables are expanded in power series in δ. The solutions of the governing equations, to $O(\delta^2)$ are again given in [16], and involve

constant G_0, G_1 and G_2. Matching by Van Dyke's method gives the following equations for the constants H_0, H_1, G_0 and G_1:

$$4E^2{H_0}^3 - 8E^2\Big(1+\frac{\Pi}{E}\Big){H_0}^2 + 4E^2\Big(1+\frac{\Pi}{E}\Big)^2 H_0 - 3 = 0 \tag{67}$$

$$H_1 = G_1 = \left(\frac{3H_D}{4E} + \frac{H_0}{E}\right) \Bigg/ \left(2 + \frac{1}{2E}\sqrt{\frac{3}{{H_0}^3}}\right) \tag{68}$$

$$G_0 = H_0 - 1 - \frac{\Pi}{E}. \tag{69}$$

The cubic in H_0 has the potential to produce three real roots. If this is the case, then the largest one is chosen, since this gives the lowest bubble pressure. This completes the determination of the matching constants to $O(\delta)$. We obtain finally the following composite expressions for the height, pressure and flux:

$$\begin{aligned}
h &= H_0 + G_0(e^{-\delta x} - 1) + \delta\left(\delta\frac{G_0}{2E}x - G_1\right)e^{-\delta x} \\
p &= \Pi + \sqrt{\frac{3}{H_0}}\exp\left(-\sqrt{\frac{3}{{H_0}^3}}x\right) \\
&\quad - \delta\left[\frac{9H_D}{4{H_0}^3}x^2 + \left(\frac{9H_1}{2{H_0}^3} - \frac{3H_D}{4}\sqrt{\frac{3}{{H_0}^3}}\right)x\right. \\
&\quad \left. - \frac{H_1}{2}\sqrt{\frac{3}{{H_0}^3}} - \frac{3H_D}{4}\right]\exp\left(-\sqrt{\frac{3}{{H_0}^3}}x\right) - \delta G_0 e^{-\delta x}; \\
Q &= H_0\left(\exp\left(-\sqrt{\frac{3}{{H_0}^3}}x\right) - 1\right) - G_0\left(e^{-\delta x} - 1\right) + \delta\left[\frac{3H_D}{4}\sqrt{\frac{3}{{H_0}^3}}x^2\right. \\
&\quad \left. + \left(\frac{3H_1}{2}\sqrt{\frac{3}{{H_0}^3}} + \frac{3H_D}{4}\right)x + H_1\right]\exp\left(-\sqrt{\frac{3}{{H_0}^3}}x\right) \\
&\quad + \delta\left(\delta\frac{G_0}{2E}x - G_1\right)e^{-\delta x}.
\end{aligned}$$

Here G_0, G_1, H_0, H_1 and H_D are all functions of E.

References

[1] Barabási, A.-L., Buldyrev, S.V., Stanley, H.E. & Suki, B., Avalanches in the lung: a statistical mechanical model, *Phys. Rev. Lett.* **76**, pp. 2192–2195, 1996.

[2] Bland, R.D., Fetal lung liquid and its removal near birth, *in* The Lung: Scientific Foundations, *ed.* Crystal, R.G. & West, J.B., pp. 2115–2127, Lippincott-Raven, 1997.

[3] Bretherton, F.P., The motion of long bubbles in tubes. *J. Fluid Mech.*, **10**, pp. 166–188, 1961.

[4] Davis, S.H. & Hocking, L., Spreading and imbibition of viscous liquid on a porous base. *Phys. Fluids* **11**, pp. 48–57, 1999.

[5] Davis, S.H. & Hocking, L., Spreading and imbibition of viscous liquid on a porous base. II. *Phys. Fluids* **12**, pp. 1646–1655, 2000.

[6] Dreyfuss, D. & Saumon, G., Ventilator-induced lung injury — lessons from experimental studies. *Am. J. Respir. Crit. Care Med.* **157**, pp. 294–323, 1998.

[7] Gaver, D.P. III, Samsel, R.W. & Solway, J., Effects of surface tension and viscosity on airway reopening, *J. Appl. Physiol.* **69**, pp. 74–85, 1990.

[8] Gaver, D.P. III, Halpern, D., Jensen, O.E. & Grotberg, J.B., The steady motion of a semi-infinite bubble through a flexible-walled channel. *J. Fluid Mech.* **319**, pp. 25–65, 1996.

[9] Grotberg, J.B., Pulmonary flow and transport phenomena. *Ann. Rev. Fluid Mech.* **26**, pp. 529–571, 1994.

[10] Grotberg, J.B., Respiratory fluid mechanics and transport processes. *Ann. Rev. Biomed. Eng.* **3**, pp. 421–457, 2001.

[11] Halpern, D. & Grotberg, J.B., Fluid-elastic instabilities of liquid-lined flexible tubes, *J. Fluid Mech.* **244**, pp. 615–632, 1992.

[12] Halpern, D. & Jensen, O.E. A semi-infinite bubble advancing into a planar tapered channel. *Phys. Fluids* **14**, pp. 431–442, 2002.

[13] Hazel, A.L. & Heil, M. Three-dimensional airway reopening: the steady propagation of a semi-infinite bubble into a buckled elastic tube. *J. Fluid Mech.* **478**, pp. 47–70, 2003.

[14] Heil, M., Minimal liquid bridges in non-axisymmetrically buckled elastic tubes, *J. Fluid Mech.* **380**, pp. 309–337, 1999.

[15] Heil, M., Finite Reynolds number effects in the propagation of an air finger into a liquid-filled flexible-walled channel, *J. Fluid Mech.* **424**, pp. 21–44, 2000.

[16] Horsburgh, M.K., Bubble propagation in flexible and permeable channels. PhD Thesis, University of Cambridge, 2000.

[17] Horsburgh, M.K. & Jensen, O.E., Bubble propagation in flexible channels with permeable walls, *in* IUTAM Symposium on Free Surface Flows, *ed.* A.C. King & Y.D. Shikmurzaev, pp. 137–144, 2001.

[18] Hsu, S.-H., Strohl, K.P. & Jamieson, A.M., Role of viscoelasticity in tube model of airway reopening. I. Non-Newtonian sols, *J. Appl. Physiol.* **76**, pp. 2841–2849, 1994.

[19] Hsu, S.-H., Strohl, K.P., Haxhiu, M.A. & Jamieson, A.M., Role of viscoelasticity in tube model of airway reopening. II. Non-Newtonian gels and airway simulation, *J. Appl. Physiol.* **80**, pp. 1649–1659, 1996.

[20] Jensen, O.E., Horsburgh, M.K., Halpern, D. & Gaver, D.P. III, The steady propagation of a bubble in a flexible-walled channel: asymptotic and computational models. *Phys. Fluids* **14**, pp. 443–457, 2002.

[21] Kamm, R.D. & Schroter, R.C., Is airway closure caused by liquid film instability? *Resp. Physiol.* **75**, pp. 141–156, 1989.

[22] Landau, L. & Levich, B., Dragging of a liquid by a moving plate. *Acta Phys-chim. URSS* **17**, pp. 42–54, 1942.

[23] Low, H.T., Chew, Y.T. & Zhou, C.W., Pulmonary airway reopening: effects of non-Newtonian fluid viscosity. *Trans. ASME J. Biomech. Engng.* **119**, pp. 298–308, 1997.

[24] Macklem, P.T., Proctor, D.F. & Hogg, J.C., The instability of peripheral airways, *Resp. Physiol.* **8**, pp. 191–203, 1970.

[25] Matsui, H., Davis, C.W., Tarran, R. & Boucher, R.C., Osmotic water permeabilities of cultured, well-differentiated normal and cystic fibrosis airway epithelia, *J. Clin. Invest.* **105**, pp. 1419–1427, 2000.

[26] McEwan, A.D. & Taylor, G.I., The peeling of a flexible strip attached by a viscous adhesive. *J. Fluid Mech.* **26**, pp. 1–15, 1966.

[27] Naire, S. & Jensen, O.E. An asymptotic model of unsteady airway reopening. *Trans. ASME J. Biomech. Engng.* (to appear), 2003.

[28] Naureckas, E.T., Dawson, C.A., Gerber, B.S., Gaver, D.P. III, Gerber, H.L., Linehan, J.H., Solway, J. & Samsel, R.W., Airway reopening pressure in isolated rat lungs, *J. Appl. Physiol.* **76**, pp. 1372–1377, 1994.

[29] Neogi, P. & Miller, C.A. Spreading kinetics of a drop on a rough solid surface. *J. Colloid Interface Sci.* **92**, 338–349, 1983.

[30] Perun, M.L. & Gaver, D.P III, An experimental model investigation of the opening of a collapsed untethered pulmonary airway, *Trans. ASME J. Biomech. Engng.* **117**, pp. 245–253, 1995

[31] Perun, M.L. & Gaver, D.P III, Interaction between airway lining fluid forces and parenchymal tethering during pulmonary airway reopening, *J. Appl. Physiol.* **79**, pp. 1717–1728, 1995.

[32] Suki, B., Barabási, A.-L., Hantos, Z., Peták, F. & Stanley, H.E., Avalanches and power-law behaviour in lung inflation, *Nature* **368**, pp. 615–618, 1994.

[33] Suki, B., Andrade, J.S. Jr., Coughlin, M.F., Stamenović, D., Standley, H.E., Sujeer, M. & Zapperi, S., Mathematical modelling of the first inflation of degassed lungs, *Ann. Biomed. Engng.* **26**, pp. 608–617, 1998.

[34] Tio, K.-K. & Sadhal, S.S. Boundary conditions for Stokes flow near a porous membrane. *Appl. Sci. Res.* **52**, pp. 1–20, 1994.

[35] Yap, D.Y.K. & Gaver, D.P. III, The influence of surfactant on two-phase flow in a flexible-walled channel under bulk equilibrium conditions, *Phys. Fluids* **10**, pp. 1846–1863, 1998.

[36] Yap, D.Y.K., Liebkemann, W.D., Solway, J. & Gaver, D.P. III, Influences of parenchymal tethering on the reopening of closed pulmonary airways. *J. Appl. Physiol.* **76**, pp. 2095–2105, 1994.